PRAMANA
— journal of
physics

Vol. 76, No. 2
February 2011
pp. 223–239

Influence of near-edge processes in the elemental analysis using X-ray emission-based techniques

GURJEET SINGH, SUNIL KUMAR, N SINGH, J GOSWAMY and D MEHTA*
Department of Physics, Panjab University, Chandigarh 160 014, India
*Corresponding author. E-mail: dmehta@pu.ac.in

Abstract. The near-edge processes, such as X-ray absorption fine structure (XAFS) andresonant Raman scattering (RRS), are not incorporated in the available theoretical attenuation coefficients, which are known to be reliable at energies away from the shell/subshell ionization thresholds of the attenuator element. Theoretical coefficients are generally used to estimate matrix corrections in routine quantitative elemental analysis based on various X-ray emission techniques. A tabulation of characteristic X-ray energies across the periodic table is provided where those X-rays are expected to alter the attenuation coefficients due to XAFS from a particular shell/subshell of the attenuator element. The influence of XAFS to the attenuation coefficient depends upon the atomic environment and the photoelectron wave vector, i.e., difference in energies of incident X-ray and the shell/subshell ionization threshold of the attenuator element. Further, the XAFS at a shell/subshell will significantly alter the total attenuation coefficient if the jump ratio at that shell/subshell is large, e.g., the K shell, L_3 subshell and M_5 subshell. The tabulations can be considered as guidelines so as to know what can be expected due to XAFS in typical photon-induced X-ray emission spectrometry.

Keywords. X-ray absorption fine structure; resonant Raman scattering; characteristic X-ray; attenuation coefficient; X-ray emission-based techniques.

PACS Nos 78.70.Dm; 61.05.cj; 87.64.kd; 32.30.Rj

1. Introduction

The near-edge processes, such as resonant Raman scattering (RRS) [1,2] and X-ray absorption fine structure (XAFS) [3–5], alter attenuation of the X-rays in the vicinity of ionization threshold of the attenuator element. These processes depend on the density of electronic states, molecular bonding and other solid-state properties of the attenuator element. With the availability of intense tuneable synchrotron sources with resolution better than 1 eV, the RRS and XAFS processes have received major impetus in recent years and are emerging as rich diagnostic tools for condensed matter systems [6–11]. The RRS process exhibits resonant behaviour for the incident photon energy (E_{in}) approaching an inner shell/subshell ionization threshold (B_i) of the atom from lower vicinity. In this process, the electrons from the lower tail of an inner shell/subshell Lorentzian distribution

are excited above the Fermi level and a virtual hole is created, which is subsequently filled by an electron of a higher shell resulting in a radiative or nonradiative transition. The K-L_2 RRS process is schematically shown in figure 1a. The RRS results in positive deviation from the available theoretical attenuation coefficients [13–15]. The solid-state effects on RRS were studied by various investigators [9–11] using tuneable synchrotron source. Nakai *et al* [11] measured the radiative emission spectra across the L_3 absorption

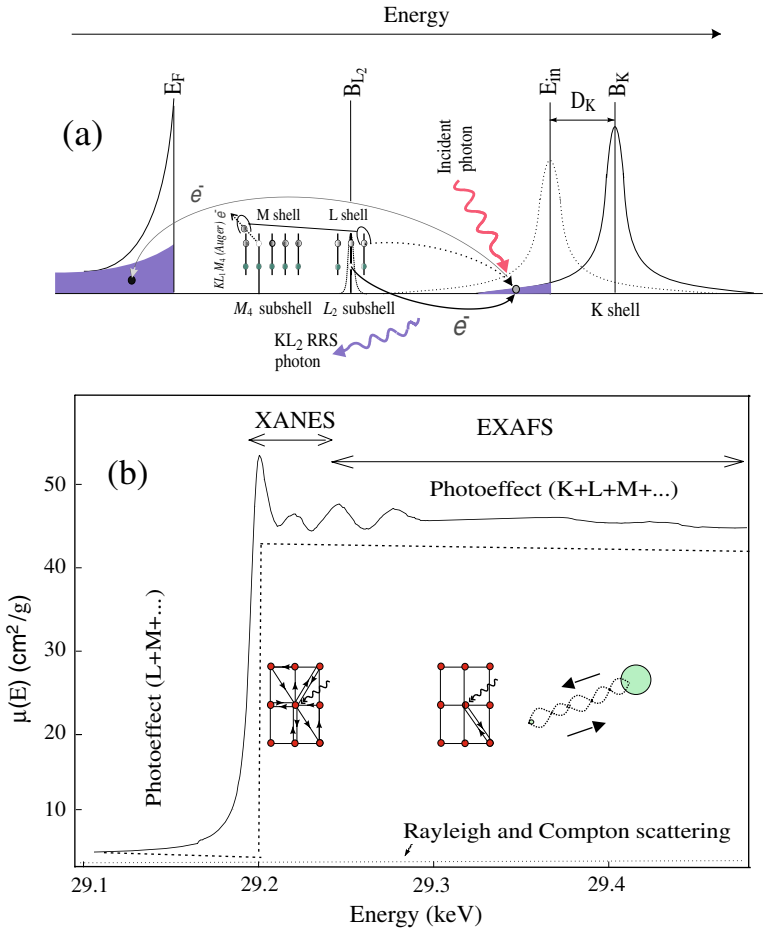

Figure 1. (**a**) Schematic representation of the RRS process induced by the incident photons of energy (E_{in}) less than the K shell binding energy (B_K) of the attenuator element. The K shell electron from the lower energy tail of Lorentzian profile is excited above the Fermi level (E_F) resulting in a virtual K shell hole state. Its typical decay channels, viz., the radiative K-L_2 and Auger KL_1M_4 resonant Raman scattering are shown. (**b**) Details of the measured mass attenuation coefficients (solid line) in $_{50}$Sn [12] plotted in the region of XAFS. The XCOM values [13] (dashed line) exhibit significant differences from the measured values.

threshold in $_{39}$Y metal and its insulator compounds. The intensity of the RRS below the ionization threshold was found to be considerably higher compared to the fluorescent Lα X-ray emission above the ionization threshold for the insulator compounds. Raman peak was also observed up to about 20 eV above the absorption peak with decreasing intensity. In the metal form, the RRS intensity was weaker. These observations were explained on the basis of band structure of the compounds using Mizouchi's four-band model [16].

Fine structure in the X-ray absorption spectrum (XAFS) occurs at the incident photon energy (E_{in}) in the upper vicinity of the shell/subshell ionization threshold of atoms embedded in lattice. The low kinetic energy photoelectrons emitted by photoeffect can return to the absorbing atom after multiple scattering among the electrons of nonexcited surrounding atoms. The low kinetic energy photoelectrons emitted by photoeffect are elastically scattered from the electrons of nonexcited surrounding atoms. These photoelectrons can return to the absorbing atom after multiple scattering, while the core–hole (lifetime $\sim 10^{-15}$ s) is still alive. An interference effect between the outgoing and backscattered photoelectron waves modulates the amplitude of the photoelectron wave function at the absorption site, and leads to the oscillatory behaviour in the attenuation coefficients at photon energies in the upper vicinity of the ionization threshold [3,4]. The phase and amplitude of interference is related to the type and location of the neighbouring atom with respect to the incident atom (interatomic distance (R)) and the photoelectron wave vector (**k**). The **k** vector is related to the difference, D_i, in binding energy of the electron (B_i) and the energy of the incident photon (E_{in}), as $k = [(2m/\hbar^2)(E_{\text{in}} - B_i)]^{1/2}$. The photoelectron has just enough kinetic energy ($0 < k < 2/R$) to be able to escape into the continuum and is strongly backscattered by the multiple neighbouring atoms. This part of the spectrum, known as X-ray absorption near edge structure (XANES), is sensitive to the electronic structure of the local vicinity of the absorbing atom species, i.e. the chemical environment. For the high kinetic energy photoelectron ($k > 2/R$), weak backscattering occurs in a single scattering process involving only one neighbour atom. This part of the spectrum known as extended X-ray absorption fine structure (EXAFS), gives information regarding the number, kind and distances of the atoms from each other and the absorber atom. XAFS does not require long-range order, but it requires short-ranged (10–50 Å) correlations between atoms, e.g. liquids, amorphous solids. The time scale for XAFS is $\sim 10^{-15}$ s, which is much faster than any atomic motion (time scale $\sim 10^{-13}$ s) involving phonons of meV energies.

Recently, absolute X-ray attenuation measurements for $_{29}$Cu [17], $_{30}$Zn [18], $_{47}$Ag [19], $_{42}$Mo [20] and $_{50}$Sn [12], in the region around the K-edge, and $_{74}$W and $_{73}$Ta [21], in the region of the M_i ($i = 1$–5) edges, have been performed using state-of-the-art extended-range technique (XERT). Significantly large differences have been reported from the theoretical values [13] in the XAFS region (figure 1b). Also, the measured attenuation coefficients [22–24] for the characteristic K/L X-rays with energies in the vicinity of the K-shell/L_i subshell ($i = 1$–3) ionization threshold ($B_{\text{K}}/B_{\text{L}_i}$) are found to deviate significantly from the theoretical values in medium and high-Z attenuator elements, and the observed alteration is attributed to the XAFS and RRS processes.

The influence of the near-edge processes has been recognized in the X-ray emission spectrometry particularly in routine elemental analysis of samples. The attenuation coefficient of the emitted characteristic X-rays will also be modified because of other elements present in the sample matrix exhibiting near-edge effects, which results in erroneous

estimates for the matrix effects and hampers reliable quantification of the trace elements in samples. The X-ray-based measurements are significantly affected for compounds like lanthanum manganite perovskite $La_{1-x}A_xMnO_3$ (A = $_{20}$Ca, $_{38}$Sr, $_{56}$Ba) [25], which have potential applications of colossal magnetoresistance. Both the RRS and XAFS due to La-L_2 subshell are expected to modify the attenuation coefficients for the emitted Mn Kα_2 and Kα_1 X-rays, respectively. The Mn-Kα_2 X-ray is ∼3 eV below and the Kα_1 X-ray is ∼8 eV above the L_2 subshell binding energy of $_{57}$La in its elemental form. The L_2M radiative RRS in $_{57}$La will result in peaks which overlap with the fluorescent L_2 subshell X-ray peaks [22].

In the present work, attention is drawn to explore possible alteration in attenuation of the characteristic X-rays due to the XAFS and recognize its influence in the accurate elemental analysis. A tabulation of characteristic X-ray energies across the periodic table is presented where the X-ray energies are expected to result in significant alteration in the attenuation coefficients due to XAFS from a subshell of some specific attenuator element. Similar tabulations for cases, where the RRS contribution is expected to be significant, have been reported recently by us [26].

2. Compilation procedure and discussion

Details of the XAFS in various elements in solid form are extracted by comparing the measured values with the theoretical base lines, i.e., the free-atom calculations which are of course not expected to include absorption fine structure (figure 1b). XAFS at a shell/subshell modifies the photoeffect contribution from the same shell/subshell. Significantly large differences of ∼10–20% have been observed for the absolute measurements performed using XERT technique [12,17–21] in the region around the shell/subshell binding energies. As the contributions of the Rayleigh and Compton scattering processes are small, jump ratio value at a shell/subshell can be taken as a measure of the fractional photoelectric contribution of that shell/subshell to the total attenuation coefficient, i.e., influence of XAFS at a shell/subshell will appear significantly in total attenuation coefficient for large jump ratio values. A plot of the jump ratio values [13] for various shell/subshells is given in figure 2a. The K shell, L_3 subshell and M_5 subshell jump ratio is large, viz., 11.7 at $Z = 11$, 5.4 at $Z = 29$ and 3.6 at $Z = 60$, respectively, and these values decrease with atomic number (Z) to 3.6, 2.3 and 2.4, respectively, at $Z = 92$. The jump ratio values are nearly constant at ∼1.4 for the L_2 and M_4 subshells and ∼1.1 for the L_1, M_1, M_2 and M_3 subshells for the range of elements shown in figure 2a. Therefore, the XAFS for the L_i ($i = 1,2$), and M_i ($i = 1$–4) subshells can cause only small alteration in the overall attenuation coefficients.

A tabulation of characteristic X-ray energies across the periodic table is given in table 1, where those X-rays are expected to undergo XAFS from a particular subshell of another attenuator element and result in significant alteration in the attenuation coefficient. The characteristic X-rays from the K shell, viz., Kα_2 (K-L_2), Kα_1 (K-L_3) and Kβ_1 (K-M_3); the L_1 subshell, viz., Lβ_4 (L_1-M_2) and Lβ_3 (L_1-M_3); the L_2 subshell, viz., Lβ_1 (L_2-M_4) and Lγ_1 (L_2-N_4); and the L_3 subshell, viz., Lα_1(L_3-M_5) and Lβ_2 (L_3-N_5); of different fluorescent elements with $11 \leq Z \leq 98$ have been chosen when their energy is lower by less than a limiting value, $D_{\text{lim}}^{\text{K/L}_i/\text{M}_i}$, than the K shell/$L_i$ ($i = 1$–3) subshell/M_i ($i = 1$–5)

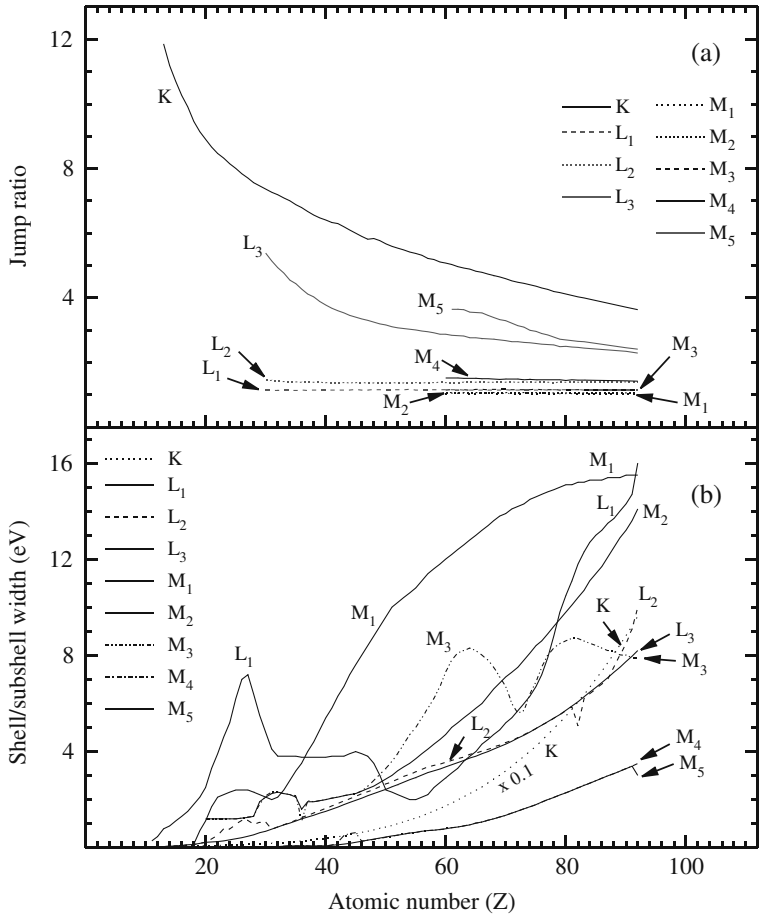

Figure 2. The plots of (**a**) jump ratio [13] and (**b**) Lorentzian width for the K shell, and the L_i (i = 1–3) and M_i (i = 1–5) subshells [30] as a function of atomic number.

subshell ionization threshold of another attenuator element. For these tabulations, the X-ray energies and the shell/subshell binding energies of elements in their free elemental form were taken from [27]. The X-ray energy values rounded off to three decimal places are given in table 1. The characteristic K shell and L_i subshell X-rays with energies above ∼1 keV, i.e., from the elements in the range Z = 11–92 and 30–92, respectively, are included in table 1. The characteristic X-rays from the M and higher shells are not considered as these have significantly low fluorescence yields [28] and result in complex X-ray spectrum. These X-rays are generally not used for multielemental analysis. XAFS generally result in first maxima within 20 eV above the ionization threshold followed by oscillations of smaller amplitude. The elements with Z = 43, 61, 84–89, 91, and the inert monoatomic gases are excluded from the list of attenuator elements. Chemical shifts and other solid-state effects can decrease binding energies of the subshells by up to ∼10 eV.

Table 1. A list of pairs of the characteristic X-ray and the attenuator element shell/subshell across the periodic table where XAFS can alter the X-ray attenuation significantly. The difference (D_i) of the X-ray energy (E_{in}) and the shell/subshell ionization threshold (B_i) in eV, is given in column 4.

Characteristic X-ray		Attenuator element	D_i (eV)
Element	Energy (E_{in}) (keV) [27]	Shell/subshell	
K-shell X-rays			
$_{11}$Na-K$\alpha_{1,2}$	1.041	$_{30}$Zn-L_3	21
$_{12}$Mg-K$\alpha_{1,2}$	1.254	$_{32}$Ge-L_2	6
		$_{32}$Ge-L_3	37
		$_{59}$Pr-M_3	11
		$_{65}$Tb-M_5	12
$_{13}$Al-K$\alpha_{1,2}$	1.487	$_{34}$Se-L_2	11
		$_{34}$Se-L_3	51
		$_{63}$Eu-M_3	6
		$_{69}$Tm-M_5	19
$_{13}$Al-Kβ_1	1.554	$_{35}$Br-L_3	4
		$_{62}$Sm-M_2	13
		$_{64}$Gd-M_3	10
		$_{70}$Yb-M_5	26
$_{14}$Si-K$\alpha_{1,2}$	1.740	$_{62}$Sm-M_1	17
		$_{72}$Hf-M_4	24
		$_{73}$Ta-M_5	5
$_{14}$Si-Kβ_1	1.836	$_{37}$Rb-L_3	31
		$_{74}$W-M_5	27
$_{15}$P-K$\alpha_{1,2}$	2.010	$_{38}$Sr-L_2	3
		$_{38}$Sr-L_3	71
		$_{68}$Er-M_2	4
		$_{76}$Os-M_5	50
$_{15}$P-Kβ_1	2.136	$_{39}$Y-L_3	56
		$_{77}$Ir-M_4	19
		$_{78}$Pt-M_5	15
$_{16}$S-Kα_1	2.308	$_{40}$Zr-L_2	1
$_{16}$S-Kα_1	2.308	$_{69}$Tm-M_1	1
$_{16}$S-K$\alpha_{1,2}$	2.308	$_{40}$Zr-L_3	85
		$_{79}$Au-M_4	17
		$_{80}$Hg-M_5	13
$_{16}$S-Kβ_1	2.464	$_{76}$Os-M_3	7

Table 1. *Continued.*

Characteristic X-ray		Attenuator element	D_i (eV)
Element	Energy (E_{in}) (keV) [27]	Shell/subshell	
$_{17}$Cl-K$\alpha_{1,2}$	2.622	$_{72}$Hf-M$_1$	22
		$_{83}$Bi-M$_5$	43
$_{18}$Ar-Kα_1	2.957	$_{81}$Tl-M$_3$	1
$_{18}$Ar-Kβ_1	3.190	$_{46}$Pd-L$_3$	17
		$_{77}$Ir-M$_1$	17
		$_{83}$Bi-M$_3$	13
$_{19}$K-K$\alpha_{1,2}$	3.311	$_{78}$Pt-M$_1$	14
$_{19}$K-Kβ_1	3.590	$_{92}$U-M$_5$	40
$_{20}$Ca-K$\alpha_{1,2}$	3.692	$_{19}$K-K	84
$_{20}$Ca-Kβ_1	4.013	$_{83}$Bi-M$_1$	14
$_{21}$Sc-Kα_2	4.086	$_{20}$Ca-K	48
$_{21}$Sc-Kα_1	4.091	$_{20}$Ca-K	53
$_{22}$Ti-Kα_2	4.505	$_{21}$Sc-K	12
$_{22}$Ti-Kα_1	4.512	$_{21}$Sc-K	18
$_{23}$V-Kα_2	4.945	$_{52}$Te-L$_1$	5
$_{23}$V-Kα_1	4.952	$_{52}$Te-L$_1$	13
$_{25}$Mn-Kα_1	5.899	$_{57}$La-L$_2$	8
$_{25}$Mn-Kβ_1	6.490	$_{61}$Pm-L$_3$	31
$_{28}$Ni-Kβ_1	8.265	$_{65}$Tb-L$_2$	13
$_{30}$Zn-Kβ_1	9.572	$_{72}$Hf-L$_3$	11
$_{31}$Ga-Kα_1	9.252	$_{71}$Lu-L$_3$	8
$_{31}$Ga-Kβ_2	10.366	$_{71}$Lu-L$_2$	18
$_{32}$Ge-Kα_1	9.886	$_{73}$Ta-L$_3$	5
$_{33}$As-Kα_1	10.544	$_{75}$Re-L$_3$	8
$_{34}$Se-Kα_2	11.182	$_{32}$Ge-K	79
$_{34}$Se-Kα_1	11.222	$_{77}$Ir-L$_3$	7
$_{35}$Br-Kα_2	11.878	$_{33}$As-K	11
$_{35}$Br-Kα_1	11.924	$_{33}$As-K	57
		$_{79}$Au-L$_3$	5
$_{35}$Br-Kβ_1	13.292	$_{78}$Pt-L$_2$	20
$_{35}$Br-Kβ_2	13.468	$_{83}$Bi-L$_3$	50
$_{45}$Rh-Kα_2	20.074	$_{42}$Mo-K	74
$_{47}$Ag-Kα_1	22.163	$_{44}$Ru-K	46
$_{56}$Ba-Kα_2	31.817	$_{52}$Te-K	3
$_{59}$Pr-Kα_1	36.026	$_{55}$Cs-K	42
$_{67}$Ho-Kβ_1	53.876	$_{66}$Dy-K	88

Table 1. *Continued.*

Characteristic X-ray		Attenuator element	D_i (eV)
Element	Energy (E_{in}) (keV) [27]	Shell/subshell	
$_{68}$Er-Kβ_1	55.674	$_{67}$Ho-K	56
$_{69}$Tm-Kβ_1	57.505	$_{68}$Er-K	20
$_{73}$Ta-Kα_1	57.535	$_{68}$Er-K	50
L_1 subshell X-rays			
$_{50}$Sn-Lβ_4	3.708	$_{81}$Tl-M$_1$	4
		$_{83}$Bi-M$_2$	12
$_{50}$Sn-Lβ_3	3.750	$_{49}$In-L$_3$	20
		$_{92}$U-M$_4$	24
$_{51}$Sb-Lβ_3	3.933	$_{50}$Sn-L$_3$	4
$_{52}$Te-Lβ_4	4.069	$_{20}$Ca-K	31
$_{52}$Te-Lβ_3	4.120	$_{20}$Ca-K	82
$_{53}$I-L β_4	4.258	$_{49}$In-L$_1$	20
$_{53}$I-L β_3	4.313	$_{92}$U-M$_3$	10
$_{54}$Xe-Lβ_3	4.512	$_{21}$Sc-K	19
$_{55}$Cs-Lβ_3	4.717	$_{51}$Sb-L$_1$	18
$_{56}$Ba-Lβ_4	4.852	$_{53}$I-L$_2$	0
$_{57}$La-Lβ_4	5.062	$_{22}$Ti-K	95
		$_{55}$Cs-L$_3$	50
$_{58}$Ce-Lβ_4	5.276	$_{56}$Ba-L$_3$	29
$_{58}$Ce-Lβ_3	5.363	$_{55}$Cs-L$_2$	4
$_{59}$Pr-Lβ_4	5.497	$_{23}$V-K	32
		$_{57}$La-L$_3$	15
$_{60}$Nd-Lβ_4	5.723	$_{55}$Cs-L$_1$	9
$_{61}$Pm-Lβ_3	6.071	$_{24}$Cr-K	82
$_{63}$Eu-Lβ_3	6.571	$_{25}$Mn-K	32
$_{66}$Dy-Lβ_4	7.204	$_{26}$Fe-K	92
$_{68}$Er-Lβ_4	7.745	$_{27}$Co-K	37
$_{68}$Er-Lβ_4	7.745	$_{62}$Sm-L$_1$	9
$_{68}$Er-Lβ_3	7.939	$_{64}$Gd-L$_2$	9
$_{78}$Pt-Lβ_3	11.235	$_{77}$Ir-L$_3$	20
$_{79}$Au-Lβ_3	11.610	$_{78}$Pt-L$_3$	46
$_{80}$Hg-Lβ_4	11.561	$_{74}$W-L$_2$	17
$_{81}$Tl-Lβ_4	11.931	$_{33}$As-K	64
		$_{79}$Au-L$_3$	12
$_{81}$Tl-Lβ_3	12.390	$_{76}$Os-L$_2$	5
$_{82}$Pb-Lβ_4	12.307	$_{80}$Hg-L$_3$	23

Table 1. *Continued.*

Characteristic X-ray		Attenuator element	D_i (eV)
Element	Energy (E_{in}) (keV) [27]	Shell/subshell	
$_{83}$Bi-Lβ_4	12.691	$_{34}$Se-K	33
		$_{81}$Tl-L$_3$	34
$_{84}$Po-Lβ_4	13.084	$_{82}$Pb-L$_3$	49
$_{85}$At-Lβ_4	13.488	$_{35}$Br-K	14
$_{86}$Rn-Lβ_4	13.898	$_{78}$Pt-L$_1$	18
$_{93}$Np-Lβ_4	17.061	$_{39}$Y-K	23
$_{95}$Am-Lβ_4	18.069	$_{40}$Zr-K	71
L_2 subshell X-rays			
$_{31}$Ga-Lβ_1	1.125	$_{11}$Na-K	53
		$_{31}$Ga-L$_3$	10
		$_{57}$La-M$_3$	2
		$_{62}$Sm-M$_4$	19
		$_{62}$Sm-M$_5$	45
$_{32}$Ge-Lβ_1	1.219	$_{32}$Ge-L$_3$	2
		$_{55}$Cs-M$_1$	2
		$_{57}$La-M$_2$	15
		$_{64}$Gd-M$_4$	2
		$_{64}$Gd-M$_5$	34
$_{33}$As-Lβ_1	1.317	$_{12}$Mg-K	12
		$_{31}$Ga-L$_1$	20
		$_{60}$Nd-M$_3$	20
		$_{66}$Dy-M$_5$	23
$_{34}$Se-Lβ_1	1.419	$_{32}$Ge-L$_1$	5
		$_{33}$As-L$_3$	96
		$_{60}$Nd-M$_2$	17
		$_{67}$Ho-M$_4$	28
		$_{68}$Er-M$_5$	10
$_{35}$Br-Lβ_1	1.526	$_{34}$Se-L$_3$	90
		$_{59}$Pr-M$_1$	15
		$_{69}$Tm-M$_4$	11
$_{36}$Kr-Lβ_1	1.632	$_{13}$Al-K	73
		$_{35}$Br-L$_3$	82
		$_{63}$Eu-M$_2$	18
		$_{71}$Lu-M$_5$	44
$_{37}$Rb-Lβ_1	1.752	$_{67}$Ho-M$_3$	11
		$_{73}$Ta-M$_5$	17

Table 1. *Continued.*

Characteristic X-ray		Attenuator element	D_i (eV)
Element	Energy (E_{in}) (keV) [27]	Shell/subshell	
$_{38}$Sr-Lβ_1	1.872	$_{14}$Si-K	33
		$_{37}$Rb-L$_2$	8
		$_{37}$Rb-L$_3$	67
		$_{74}$W-M$_4$	0
$_{39}$Y-Lβ_1	1.996	$_{38}$Sr-L$_3$	56
		$_{76}$Os-M$_5$	36
$_{40}$Zr-Lβ_1	2.124	$_{39}$Y-L$_3$	44
		$_{72}$Hf-M$_3$	17
		$_{77}$Ir-M$_4$	8
		$_{78}$Pt-M$_5$	3
$_{41}$Nb-Lβ_1	2.257	$_{40}$Zr-L$_3$	35
$_{42}$Mo-Lβ_1	2.395	$_{41}$Nb-L$_3$	24
		$_{80}$Hg-M$_4$	10
		$_{81}$Tl-M$_5$	6
$_{43}$Tc-Lβ_1	2.537	$_{16}$S-K	65
		$_{40}$Zr-L$_1$	5
		$_{42}$Mo-L$_3$	17
$_{44}$Ru-Lβ_1	2.683	$_{43}$Tc-L$_3$	6
		$_{75}$Re-M$_2$	2
$_{45}$Rh-Lβ_1	2.834	$_{17}$Cl-K	12
		$_{74}$W-M$_1$	15
$_{47}$Ag-Lβ_1	3.151	$_{45}$Rh-L$_2$	5
		$_{79}$Au-M$_2$	3
$_{48}$Cd-Lβ_1	3.316	$_{78}$Pt-M$_1$	19
$_{50}$Sn-Lβ_1	3.663	$_{19}$K-K	55
$_{50}$Sn-Lγ_1	4.132	$_{20}$Ca-K	94
		$_{51}$Sb-L$_3$	0
$_{51}$Sb-Lγ_1	4.349	$_{52}$Te-L$_3$	8
$_{52}$Te-Lβ_1	4.029	$_{48}$Cd-L$_1$	11
$_{52}$Te-Lγ_1	4.572	$_{21}$Sc-K	79
		$_{53}$I-L$_3$	15
$_{54}$Xe-Lγ_1	5.034	$_{22}$Ti-K	68
		$_{55}$Cs-L$_3$	22
$_{55}$Cs-Lβ_1	4.620	$_{52}$Te-L$_2$	8
$_{55}$Cs-Lγ_1	5.281	$_{56}$Ba-L$_3$	34
		$_{23}$V-K	66
$_{56}$Ba-Lγ_1	5.531	$_{57}$La-L$_3$	48

Table 1. *Continued.*

Characteristic X-ray		Attenuator element	D_i (eV)
Element	Energy (E_{in}) (keV) [27]	Shell/subshell	
$_{57}$La-Lβ_1	5.042	$_{22}$Ti-K	76
		$_{55}$Cs-L$_3$	30
$_{58}$Ce-Lβ_1	5.263	$_{56}$Ba-L$_3$	16
$_{58}$Ce-Lγ_1	6.054	$_{24}$Cr-K	65
$_{59}$Pr-Lβ_1	5.489	$_{23}$V-K	24
		$_{57}$La-L$_3$	7
$_{60}$Nd-Lβ_1	5.722	$_{55}$Cs-L$_1$	7
$_{60}$Nd-Lγ_1	6.604	$_{25}$Mn-K	65
$_{62}$Sm-Lγ_1	7.183	$_{26}$Fe-K	71
$_{63}$Eu-Lβ_1	6.456	$_{59}$Pr-L$_2$	16
$_{64}$Gd-Lγ_1	7.790	$_{27}$Co-K	81
$_{65}$Tb-Lγ_1	8.105	$_{67}$Ho-L$_3$	34
$_{66}$Dy-Lβ_1	7.248	$_{64}$Gd-L$_3$	5
$_{66}$Dy-Lγ_1	8.426	$_{28}$Ni-K	94
$_{67}$Ho-Lβ_1	7.526	$_{65}$Tb-L$_3$	12
$_{68}$Er-Lβ_1	7.811	$_{66}$Dy-L$_3$	21
$_{69}$Tm-Lβ_1	8.102	$_{67}$Ho-L$_3$	31
$_{70}$Yb-Lβ_1	8.402	$_{28}$Ni-K	69
		$_{68}$Er-L$_3$	44
$_{71}$Lu-Lβ_1	8.709	$_{65}$Tb-L$_1$	1
$_{72}$Hf-Lβ_1	9.023	$_{29}$Cu-K	44
$_{73}$Ta-Lγ_1	10.895	$_{76}$Os-L$_3$	24
$_{74}$W-Lβ_1	9.672	$_{30}$Zn-K	14
$_{74}$W-Lγ_1	11.285	$_{72}$Hf-L$_1$	15
$_{75}$Re-Lγ_1	11.685	$_{73}$Ta-L$_1$	4
$_{76}$Os-Lβ_1	10.354	$_{71}$Lu-L$_2$	6
$_{83}$Bi-Lγ_1	15.247	$_{37}$Rb-K	48
$_{84}$Po-Lβ_1	13.443	$_{83}$Bi-L$_3$	24
$^{Th}_{90}$-Lβ_1	16.202	$_{38}$Sr-K	97
L_3 subshell X-rays			
$_{30}$Zn-Lα_1	1.012	$_{28}$Ni-L$_1$	4
		$_{52}$Te-M$_1$	6
		$_{55}$Cs-M$_3$	14
		$_{60}$Nd-M$_4$	12
		$_{60}$Nd-M$_5$	34
		$_{11}$Na-K	26

Table 1. *Continued.*

Characteristic X-ray		Attenuator element	D_i (eV)
Element	Energy (E_{in}) (keV) [27]	Shell/subshell	
$_{31}$Ga-Lα_1	1.098	$_{29}$Cu-L$_1$	2
		$_{62}$Sm-M$_5$	18
$_{32}$Ge-Lα_1	1.188	$_{58}$Ce-M$_3$	3
		$_{63}$Eu-M$_4$	27
		$_{64}$Gd-M$_5$	3
$_{33}$As-Lα_1	1.282	$_{58}$Ce-M$_2$	9
		$_{65}$Tb-M$_4$	7
		$_{65}$Tb-M$_5$	41
$_{34}$Se-Lα_1	1.379	$_{57}$La-M$_1$	18
		$_{67}$Ho-M$_5$	28
$_{35}$Br-Lα_1	1.481	$_{34}$Se-L$_2$	5
		$_{34}$Se-L$_3$	45
		$_{63}$Eu-M$_3$	0
		$_{68}$Er-M$_4$	28
		$_{69}$Tm-M$_5$	13
$_{36}$Kr-Lα_1	1.581	$_{13}$Al-K	22
		$_{35}$Br-L$_3$	31
		$_{60}$Nd-M$_1$	6
		$_{70}$Yb-M$_4$	5
$_{37}$Rb-Lα_1	1.694	$_{64}$Gd-M$_2$	6
		$_{66}$Dy-M$_3$	18
		$_{72}$Hf-M$_5$	32
$_{38}$Sr-Lα_1	1.806	$_{37}$Rb-L$_3$	2
		$_{63}$Eu-M$_1$	7
		$_{73}$Ta-M$_4$	13
$_{39}$Y-Lα_1	1.923	$_{75}$Re-M$_5$	40
$_{40}$Zr-Lα_1	2.042	$_{71}$Lu-M$_3$	19
		$_{76}$Os-M$_4$	11
		$_{77}$Ir-M$_5$	2
$_{41}$Nb-Lα_1	2.166	$_{15}$P-K	20
		$_{39}$Y-L$_2$	10
		$_{78}$Pt-M$_5$	45
$_{42}$Mo-Lα_1	2.293	$_{74}$W-M$_3$	12
		$_{79}$Au-M$_4$	2
$_{43}$Tc-Lα_1	2.424	$_{81}$Tl-M$_5$	35
$_{44}$Ru-Lα_1	2.558	$_{42}$Mo-L$_3$	38
		$_{77}$Ir-M$_3$	8

Table 1. *Continued.*

Characteristic X-ray		Attenuator element	D_i (eV)
Element	Energy (E_{in}) (keV) [27]	Shell/subshell	
$_{45}$Rh-Lα_1	2.697	$_{43}$Tc-L$_3$	20
		$_{75}$Re-M$_2$	15
		$_{83}$Bi-M$_4$	9
$_{46}$Pd-Lα_1	2.839	$_{17}$Cl-K	16
		$_{44}$Ru-L$_3$	1
		$_{74}$W-M$_1$	19
$_{47}$Ag-Lα_1	2.984	$_{44}$Ru-L$_2$	18
$_{49}$In-Lα_1	3.287	$_{80}$Hg-M$_2$	9
$_{50}$Sn-Lα_1	3.444	$_{79}$Au-M$_1$	19
$_{51}$Sb-Lα_1	3.605	$_{46}$Pd-L$_1$	0
$_{51}$Sb-Lβ_2	4.101	$_{20}$Ca-K	63
$_{52}$Te-Lα_1	3.769	$_{49}$In-L$_3$	39
$_{53}$I-Lα_1	3.938	$_{50}$Sn-L$_3$	9
$_{53}$I-Lβ_2	4.507	$_{21}$Sc-K	15
$_{54}$Xe-Lα_1	4.105	$_{20}$Ca-K	67
$_{54}$Xe-Lβ_2	4.715	$_{51}$Sb-L$_1$	16
$_{56}$Ba-Lα_1	4.466	$_{50}$Sn-L$_1$	2
$_{58}$Ce-Lα_1	4.840	$_{90}$Th-M$_2$	9
$_{59}$Pr-Lα_1	5.033	$_{22}$Ti-K	67
		$_{55}$Cs-L$_3$	21
$_{62}$Sm-Lα_1	5.636	$_{56}$Ba-L$_2$	12
$_{62}$Sm-Lβ_2	6.587	$_{25}$Mn-K	48
$_{63}$Eu-Lβ_2	6.844	$_{59}$Pr-L$_1$	9
$_{64}$Gd-Lα_1	6.058	$_{24}$Cr-K	68
$_{65}$Tb-Lα_1	6.273	$_{57}$La-L$_1$	6
$_{66}$Dy-Lα_1	6.495	$_{61}$Pm-L$_3$	36
$_{66}$Dy-Lβ_2	7.636	$_{63}$Eu-L$_2$	19
$_{67}$Ho-Lα_1	6.720	$_{62}$Sm-L$_3$	4
$_{69}$Tm-Lα_1	7.180	$_{26}$Fe-K	68
$_{71}$Lu-Lβ_2	9.049	$_{29}$Cu-K	70
		$_{66}$Dy-L$_1$	3
$_{74}$W-Lα_1	8.398	$_{28}$Ni-K	65
		$_{68}$Er-L$_3$	40
$_{75}$Re-Lα_1	8.652	$_{69}$Tm-L$_3$	4
$_{77}$Ir-Lβ_2	10.920	$_{76}$Os-L$_3$	49
$_{78}$Pt-Lβ_2	11.250	$_{77}$Ir-L$_3$	35
$_{79}$Au-Lα_1	9.713	$_{30}$Zn-K	54

Table 1. *Continued.*

Characteristic X-ray		Attenuator element	D_i (eV)
Element	Energy (E_{in}) (keV) [27]	Shell/subshell	
$_{79}$Au-Lβ_2	11.585	$_{78}$Pt-L_3	21
$_{80}$Hg-Lα_1	9.989	$_{70}$Yb-L_2	11
$_{80}$Hg-Lβ_2	11.925	$_{33}$As-K	58
		$_{79}$Au-L_3	6
$_{82}$Pb-Lα_1	10.551	$_{75}$Re-L_3	16
$_{83}$Bi-Lβ_2	12.979	$_{76}$Os-L_1	11
$_{84}$Po-Lα_1	11.130	$_{32}$Ge-K	27
$_{88}$Ra-Lβ_2	14.841	$_{80}$Hg-L_1	2
$_{89}$Ac-Lβ_2	15.230	$_{37}$Rb-K	30

The XAFS effects can be avoided when the measurements are performed using elements in the form of monoatomic gas.

In view of the jump ratio values for various shell/subshells, the limiting values for the L_i ($i = 1$–3) subshells, $D_{\text{lim}}^{L_i}$, are taken to be 20, 30 and 50, respectively, and that for the M_i ($i = 1$–5) subshells, the $D_{\text{lim}}^{M_i}$, are taken to be 20, 20, 20, 30 and 50, respectively. The D_{lim}^{K} value for the K shell ionization threshold has been chosen to be 100 eV for all the elements over the range $Z = 11$–100. Same value of D_{lim}^{K} has been considered for the higher-Z elements despite decrease in the jump ratio values (figure 2a). The fluorescence yield of the L_1 subshell is smaller by a factor of ∼5–20 compared to the L_2 and L_3 subshells for the elements in the atomic region $Z = 29$–49 [28]. The L_i ($i = 1$–3) subshell X-rays are not well resolved in the spectra taken using a semiconductor detector and contribution of the L_1 subshell X-rays will be small. Therefore, the Lβ_3 and Lβ_4 X-rays for these elements are not included in table 1. Similarly, the contributions of weak Lγ_1 (L_2 subshell) and Lβ_2 (L_3 subshell) X-rays for these elements are not included as they are too small to be considered.

The characteristic L_1 and L_2 subshell X-rays having energies above the L_i ($i = 2,3$) subshell ionization threshold of the same element by less than $D_{\text{lim}}^{L_i}$ are given in table 2. Such effects are expected to be important in fluorescent measurements involving thick elemental targets [29]. These elements are not included in table 1. The intense Mβ and Mγ X-ray components exhibiting XAFS with the M_5 subshell of the same element are also included in table 2. It is worth noting that the energy difference between the M_4 and M_5 subshells is 34 eV for $Z = 65$ and it increases to 176 eV for $Z = 92$ [27].

Further, it is important to note that the finite Lorentzian energy profile of the characteristic X-rays will lead to smearing of the oscillations in the attenuation coefficients. The width of the X-ray is the sum of the widths of the levels involved in the X-ray transition (figure 2b). For smaller ($E_{\text{in}} - B_i$) energy differences, the X-ray energy profile may

Table 2. The shell/subshell of the attenuator elements that is expected to exhibit XAFS by the characteristic X-ray of the same element.

Characteristic X-ray		Attenuator element	D_i (eV)
Element	Energy (E_{in}) (keV) [27]	Shell/subshell	
L_1 subshell X-rays			
$_{34}$Se-Lβ_4	1.4857	$_{34}$Se-L$_2$	10
		$_{34}$Se-L$_3$	50
$_{34}$Se-Lβ_3	1.4920	$_{34}$Se-L$_2$	16
$_{35}$Br-Lβ_4	1.5927	$_{35}$Br-L$_3$	43
		$_{35}$Br-L$_2$	5
$_{35}$Br-Lβ_3	1.6005	$_{35}$Br-L$_3$	51
$_{37}$Rb-Lβ_4	1.8177	$_{37}$Rb-L$_3$	13
$_{37}$Rb-Lβ_3	1.8266	$_{37}$Rb-L$_3$	22
$_{38}$Sr-Lβ_3	1.9472	$_{38}$Sr-L$_3$	8
$_{77}$Ir-Lγ_2	12.8414	$_{77}$Ir-L$_2$	17
$_{78}$Pt-Lγ_2	13.2729	$_{78}$Pt-L$_2$	0
$_{82}$Pb-Lγ_3	15.2163	$_{82}$Pb-L$_2$	16
$_{88}$Ra-Lβ_3	15.4470	$_{88}$Ra-L$_3$	3
$_{95}$Am-Lγ_4	22.9790	$_{95}$Am-L$_2$	27
$_{96}$Cm-Lγ_4	23.6640	$_{96}$Cm-L$_2$	13
L_2 subshell X-rays			
$_{30}$Zn-Lβ_1	1.035	$_{30}$Zn-L$_3$	15
$_{31}$Ga-Lβ_1	1.125	$_{31}$Ga-L$_3$	10
$_{32}$Ge-Lβ_1	1.219	$_{32}$Ge-L$_3$	2
M_3 subshell X-rays			
$_{90}$Th-Mγ	3.369	$_{90}$Th-M$_5$	37
$_{92}$U-Mγ	3.567	$_{92}$U-M$_5$	15
$_{93}$Np-Mγ	3.664	$_{93}$Np-M$_5$	0
M_4 subshell X-rays			
$_{65}$Tb-Mβ	1.272	$_{65}$Tb-M$_5$	31
$_{66}$Dy-Mβ	1.328	$_{66}$Dy-M$_5$	33
$_{67}$Ho-Mβ	1.388	$_{67}$Ho-M$_5$	36
$_{68}$Er- Mβ	1.449	$_{68}$Er- M$_5$	40
$_{69}$Tm-Mβ	1.510	$_{69}$Tm-M$_5$	42
$_{70}$Yb-Mβ	1.571	$_{70}$Yb-M$_5$	43

Table 2. *Continued.*

Characteristic X-ray		Attenuator element	D_i (eV)
Element	Energy (E_{in}) (keV) [27]	Shell/subshell	
$_{71}$Lu-Mβ	1.634	$_{71}$Lu-M$_5$	43
$_{72}$Hf-Mβ	1.699	$_{72}$Hf-M$_5$	37
$_{73}$Ta-Mβ	1.765	$_{73}$Ta-M$_5$	30
$_{74}$W-Mβ	1.833	$_{74}$W-M$_5$	24
$_{75}$Re-Mβ	1.902	$_{75}$Re-M$_5$	19
$_{76}$Os-Mβ	1.977	$_{76}$Os-M$_5$	17
$_{77}$Ir-Mβ	2.052	$_{77}$Ir-M$_5$	12
$_{78}$Pt-Mβ	2.127	$_{78}$Pt-M$_5$	5

overlap with that of the shell/subshell of the attenuator. The present tabulations are offered as suggestive and not intended to be used rigorously. A systematic and precise derivation of such tabulations appears to be an intractable challenge.

If the atom is involved in chemical bonding, there will be a shift in the binding energies of the electrons from that for the free atom. The formation of chemical bonding causes migration of the valence electrons among the participating atoms, thus reducing screening effects and increasing their inner shell binding energies. This energy change (ΔE_b) may be of the order of few eV in the low- and medium-Z elements. The K shell binding energy of $_{13}$Al in Al_2O_3 and $_{14}$Si in SiO_2, $_{24}$Cr in Cr_2O_3 and $(CrO_4)^{2-}$, were measured to be higher by 5.9 and 8.0 eV [29], 7 and 15 eV [31], respectively, than that in the metallic state. If the photon energy, E_{in}, is higher by few eV than an ionization threshold of the attenuator atom in elemental form, it exhibits XAFS. If the ionization threshold of the attenuator atom in a chemical form is lower by few eV than E_{in}, it exhibits RRS. Therefore, an X-ray and attenuator combination with $D_i \sim$ few eV listed in table 1 as the case of XAFS can be the case of RRS for different chemical forms of the attenuator element.

3. Conclusions

The X-rays having energy, E_{in}, just above the K shell/L_3 subshell/M_5 subshell of the attenuator element with large jump ratio values are expected to significantly alter the attenuation coefficients due to XAFS. In light of the near-edge processes, precise measurements of the attenuation coefficients for the shortlisted fluorescent X-rays and attenuator element pairs are required to update the database of attenuation coefficients. The characteristic X-rays obtained from elemental target fluorescence or radioisotope decay have reproducible Lorentzian profile. It is interesting to further extend the measurements to different chemical and physical forms of attenuator elements, viz., the nanosize particles and the solutions of different insulator compounds.

References

[1] C J Sparks and G E Ice, *Ind. J. Phys.* **B71**, 393 (1997)
[2] S Manninen, *Radiat. Phys. Chem.* **50**, 77 (1997)
[3] A Bianconi, *X-ray absorption: Principles, applications, techniques of EXAFS, SEXAFS, XANES* edited by D C Koningsberger and R Prins (Wiley, New York, 1988) p. 1
[4] E A Stern, *Phys. Rev.* **B10**, 3027 (1974)
[5] J J Rehr, *Radiat. Phys. Chem.* **75**, 1547 (2006) and references therein
[6] J P Gomilsek, A Kodre, I Arcon and V Nemanic, *Nucl. Instrum. Methods* **B266**, 677 (2008)
[7] A Kodre, J P Gomilsek, A Mihelic and I Arcon, *Radiat. Phys. Chem.* **75**, 188 (2006)
[8] K S Hamad, R Roth, J Rockenberger, T van Buren and A P Alivisatos, *Phys. Rev. Lett.* **83**, 3464 (1999)
[9] C Dallera, M H Krisch, A Rogalev, C Gauthier, J Goulon, F Sette and A Sole, *Phys. Rev.* **B62**, 7093 (2000)
[10] H' J Sánchez, M C Valentinuzzi and C Pérez, *J. Phys. B: At. Mol. Opt.* **39**, 4317 (2006)
[11] S Nakai, Y Megawa, F Terasaki, C Gang, T Ohuchi, K Obara, T Kojima, H Arai, T Hasiwakura and Y Kitajima, *Phys. Rev.* **B61**, 7433 (2000)
[12] M D de Jonge, C Q Tran, C T Chantler, Z Barnea, B B Dhal, D Paterson, E P Kanter, S H Southworth, L Young, M A Beno, J A Linton and G Jennings, *Phys. Rev.* **A75**, 032702 (2007)
[13] M J Berger and J H Hubbell, *XCOM: Photon cross-sections database, Web Version 1.2* (National Institute of Standards and Technology, Gaitherburg, USA, 1999); available at http://physics.nist.govt/xcom, 1987/99
[14] C T Chantler, *J. Phys. Chem. Ref. Data* **24**, 71 (1995); *ibid.* **29**, 597 (2000)
[15] M J Berger and J H Hubbell, *NIST Standard Reference Database* **8**, **87**, 3597 (2004)
[16] H Mizouchi, *Phys. Rev.* **B58**, 15557 (1998)
[17] C T Chantler, C Q Tran, Z Barnea, D Paterson, D J Cookson and D X Balaic, *Phys. Rev.* **A64**, 062506 (2001)
[18] N A Rae, C T Chantler, Z Barnea, M D de Jonge, C Q Tran and J R Hester, *Phys. Rev.* **A81**, 022904 (2010)
[19] C Q Tran, C T Chantler, Z Barnea, M D de Jonge, B B Dhal, C T Y Chung, D Paterson and J Wang, *J. Phys. B: At. Mol. Opt.* **38**, 89 (2005)
[20] M D de Jonge, C Q Tran, C T Chantler, Z Barnea, B B Dhal, D J Cookson, W Lee and A Mashayekhi, *Phys. Rev.* **A71**, 032702 (2005)
[21] Z H Levine, S Grantham, C Tarrio, D J Paterson, I McNulty, T M Levin, A L Ankudinov and J J Rehr, *J. Res. Natl. Inst. Stand. Technol.* **108**, 1 (2003)
[22] V Sharma, S Kumar, D Mehta and N Singh, *Phys. Rev.* **A78**, 012507 (2008)
[23] S Kumar, V Sharma, S Kumar, M Alrakabi, D Mehta and N Singh, *J. Appl. Phys.* **105**, 104909 (2009)
[24] S Kumar, M Alarakabi, S Kumar, D Mehta, S C Bedi and N Singh, *Nucl. Instrum. Methods* **B268**, 431 (2010)
[25] R A Souza, N M Souza-Neto, A Y Ramos, H C N Tolentino and E Granado, *Phys. Rev.* **B70**, 214426 (2004)
[26] S Kumar, G Singh, S Kumar, D Mehta and N Singh, *Nucl. Instrum. Methods* **B268**, 2437 (2010)
[27] E Browne and R B Firestone, *Table of radioactive isotopes* edited by V S Shirley (Wiley, New York, 1986) p. C14
[28] J L Campbell, *At. Data Nucl. Data Tables* **85**, 291 (2003); *ibid.* **95**, 115 (2009)
[29] J Szlachetko, J Cl Dousse, M Berset, K Fennane, M Szlachetko, J Hoszowska, R Barrett, M Pajek and A Kubala-Kukus, *Phys. Rev.* **A75**, 022512 (2007)
[30] J L Campbell and T Papp, *At. Data Nucl. Data Tables* **77**, 1 (2001)
[31] A G Karydas, S Galanopoulos, Ch Zarkadas, T Paradellis and N Kallithrakas-Kontos, *J. Phys. Condens. Matter* **14**, 12367 (2002)